Modeling of Solid-Oxide Electrolyser Cells: From H₂, CO Electrolysis to Co-Electrolysis

V. Menon[a], V. M. Janardhanan[b], and O. Deutschmann[c]

[a] Institute for Chemical Technology and Polymer Chemistry, Karlsruhe Institute of Technology (KIT), 76131 Karlsruhe, Germany
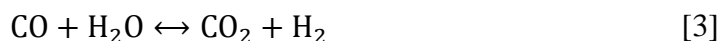[b] Department of Chemical Engineering, IIT Hyderabad, Yeddumailaram, Andhra Pradesh 502 205, India
[c] Institute for Catalysis Research and Technology, Karlsruhe Institute of Technology (KIT), 76131 Karlsruhe, Germany

In this analysis, we report an in-house model to describe the complex fundamental and functional interactions between various internal physico-chemical phenomena of a SOEC. Electrochemistry at the three-phase boundary is modeled using a modified Butler-Volmer approach that considers H_2 and CO, individually, as electrochemically active species. Also, a multi-step elementary heterogeneous reaction mechanism for the thermo-catalytic H_2/CO_2 electrode chemistry, along with the dusty gas model (DGM) to account for multi-component diffusion of ideal gases through porous media, are used. The model is geometry independent. Results pertaining to detailed chemical processes within the cathode, electrochemical behavior and irreversible losses during SOEC operation are demonstrated.

Introduction

High temperature co-electrolysis of H_2O and CO_2 offers a promising means for syngas production via efficient use of heat and electricity (1-3). Some of the considerable advantages to this technology include high reaction kinetics, reduced cell resistance, lowered probability of carbon formation, possibility of coupling with Fischer-Tropsch process for conversion of syngas to liquid fuel/hydrocarbons, effective utilization of heat from exothermic water-gas shift reaction and less complexity at the systems level due to the lack of need for a separate water-gas shift reactor. In a solid oxide electrolyzer cell (SOEC), three common reactions take place simultaneously - CO_2 electrolysis, H_2O electrolysis, and reverse water-gas shift reaction. The electrolysis reactions that contribute to the production of H_2 and CO occur at the cathode three-phase boundary (TPB) via Eqs. [1] and [2], where as the reverse water-gas shift reaction occurs in the porous cathode material via Eq. [3], as follows:

$$H_2O + 2e^- \longrightarrow H_2 + O^{2-} \qquad [1]$$

$$CO_2 + 2e^- \longrightarrow CO + O^{2-} \qquad [2]$$

$$CO + H_2O \longleftrightarrow CO_2 + H_2 \qquad [3]$$

The schematic representation of a co-flow planar SOEC is shown in Figure 1. The white arrows represent the direction of fluxes, while the horizontal arrows represent the direction of flow in the gas channels. In this article, an electrochemical model to study the V-I characteristics and irreversible loss behavior of a SOEC is demonstrated. Unlike approximations made in literature, Butler-Volmer equations based on single step electron charge transfer reactions, are employed for both CO_2 and H_2O electrolysis (4, 5).
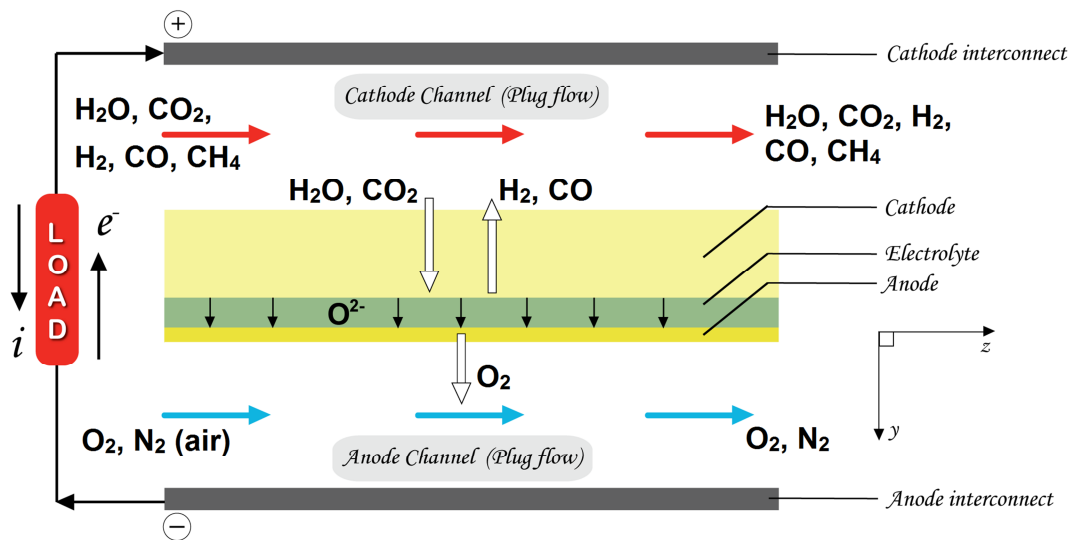
Figure 1. Schematic depiction of a planar SOEC.

Modeling Approach

Electrochemical Model

The charge transfer chemistry occurs at the three-phases boundaries (TPB), which are basically interfaces formed by the electro-catalyst, electrolyte and gas-phase boundaries. In this study, we only consider charge transfer occurring at the electrode-electrolyte interface and not across the utilization region of the electrodes. The potential balance equations are formulated after taking into account all the irreversibilities that occur during operation, with respect to electrochemically active species - H_2 and CO, and are given by

$$E_{cell} = E_{rev,H2} + |\eta_a(i_{H2})| + \eta_c(i_{H2}) + \eta_{ohm}(i_{H2}) + \eta_{conc}(i_{H2}) \qquad [4]$$

$$E_{cell} = E_{rev,CO} + |\eta_a(i_{CO})| + \eta_c(i_{CO}) + \eta_{ohm}(i_{CO}) + \eta_{conc}(i_{CO}) \qquad [5]$$

where η_a and η_c are the activation overpotentials at the anode and cathode respectively, η_{ohm} is the ohmic overpotential, and η_{conc} is the concentration overpotential. The concentration overpotential is not treated explicitly as porous media transport is modeled in detail. E_{rev} is the 'reversible' cell voltage, which is the maximum possible potential that can be derived from a cell operating reversibly, and is given by the Nernst equation as

$$E_{rev,H2} = E_{H2}^0 + \frac{RT}{2F} \ln \left(\frac{p_{H_2,c} p_{O_2,a}^{1/2}}{p_{H_2O,c}} \right) \qquad [6]$$

$$E_{rev,CO} = E_{CO}^0 + \frac{RT}{2F} \ln \left(\frac{p_{CO,c} p_{O_2,a}^{1/2}}{p_{CO_2,c}} \right) \qquad [7]$$

where E^0 is the electromotive force (EMF) at standard pressure, p_i represents the partial pressures of H_2, H_2O (at the cathode TPB) and O_2 (at the anode TPB). The temperature dependent E^0 is calculated from thermodynamic data ($\Delta G/2F$). The ohmic overpotential in Eqs. [4] and [5] is given by

$$\eta_{ohm} = R_{tot} i \qquad [8]$$

where R_{tot} is given by

$$R_{tot} = R_e + R_c + R_{LSM} + R_{Ni-YSZ} \qquad [9]$$

The magnitudes of these resistances depend on the type of material used and the micro-structure of the porous electrode. In modern cells, the electronic resistances of both electrodes R_{LSM}, R_{Ni-YSZ} and the contact resistances between solid-solid interfaces R_c are negligible compared to the ionic resistance of the electrolyte R_e, which is given by

$$R_e = \frac{l_e}{\sigma_e} \qquad [10]$$

where l_e is the thickness of the electrolyte, and σ_e is the electrolyte conductivity, with the SI unit – S/m, which varies as a strong function of temperature as

$$\sigma_e = (3.34 \times 10^4 \frac{S}{m}) \times exp \left(-\frac{10300K}{T} \right) \qquad [11]$$

The Butler-Volmer equation is used to describe the functional relationship between the activation losses and current density. For the H_2 electrode, this takes the form (4)

$$i_{H_2} = i_{0,H_2} \left[exp \left(\frac{(1+\beta_a)F\eta_c}{RT} \right) - exp \left(-\frac{\beta_c F\eta_c}{RT} \right) \right] \qquad [12]$$

For the CO_2 electrode, the B-V equation for the electrochemical reduction of CO_2 is (5)

$$i_{CO} = i_{0,CO} \left[exp \left(\frac{\beta_a F\eta_c}{RT} \right) - exp \left(-\frac{(1+\beta_c)F\eta_c}{RT} \right) \right] \qquad [13]$$

One may also refer to (5) for the detailed description and derivation of the B-V equation for CO_2 electrolysis. For the O_2 electrode, the B-V equation can be described as (4)

$$i_i = i_{0,O_2} \left[exp\left(\frac{\beta_a F \eta_a}{RT}\right) - exp\left(-\frac{\beta_c F \eta_a}{RT}\right) \right] \qquad [14]$$

where i is the current, i_0 is the exchange current density, η is the activation overpotential, F is the Faraday constant, T is the temperature and β is the asymmetric charge transfer coefficient. The subscript index i refers to either H_2 or CO. The exchange current densities $i_{0,H2}$, $i_{0,CO}$ and $i_{0,O2}$ are expressed as:

$$i_{0,H_2} = i_{H_2}^* \frac{\left(p_{H_2}/p_{H_2}^*\right)^{1/4} \left(p_{H_2O}\right)^{3/4}}{1 + \left(p_{H_2}/p_{H_2}^*\right)^{1/2}} \qquad [15]$$

$$i_{0,CO} = i_{CO}^* \frac{\left(p_{CO_2}/p_{CO}\right)^{1/4}}{1 + \left(p_{CO}/p_{CO}^*\right) + \left(p_{CO_2}/p_{CO_2}^*\right)} \qquad [16]$$

$$i_{0,O_2} = i_{O_2}^* \frac{\left(p_{O_2}/p_{O_2}^*\right)^{1/4}}{1 + \left(p_{O_2}/p_{O_2}^*\right)^{1/2}} \qquad [17]$$

where p is the partial pressure and p^* is the equilibrium pressure. The formulae for these parameters can be found in (4, 5). An Arrhenius expression is used to describe the temperature dependence of exchange current density in the form of i^*, which is given by

$$i_i^* = k_i \, exp\left(-\frac{E_i}{RT}\right) \qquad [18]$$

where the subscript index i refers to either H_2, CO or O_2. Due to the fact that the TPB sites are shared by both H_2O and CO_2, a factor γ is introduced to normalize the net current density and account for the relative percentages of H_2O and CO_2 at the electrode-electrolyte interface. Therefore, the net current density reduces to

$$i = I_{H_2} + I_{CO} = \gamma i_{H_2} + (1 - \gamma)i_{CO}, \qquad \gamma = \frac{Y_{H_2O}^{TPB}}{\left(Y_{H_2O}^{TPB} + Y_{CO_2}^{TPB}\right)} \qquad [19]$$

Multi-Component Mass Transport in Porous Media

Due to geometrical considerations, the reaction diffusion equation for species transport in the electrodes is described in 1D along its thickness. This is given by

$$\frac{\partial(\phi \rho_f Y_k)}{\partial t} = -\frac{\partial(J_k)}{\partial y} + \dot{s}_k W_k A_s \qquad [20]$$

Total density of the mixture can be calculated from

$$\frac{\partial(\phi \rho_f)}{\partial t} = -\sum_{k=1}^{K_g} \frac{\partial(J_k)}{\partial y} + \sum_{k=1}^{K_g} \dot{s}_k W_k A_s \qquad [21]$$

Here, t is the time, ϕ is the porosity, Y_k is the species mass fraction of species k, $\dot{s}_k$ is the heterogeneous molar production rate of the chemical species k, ρ_f is the fluid density, W_k is the species molecular weight, y is the independent spatial variable along the thickness, and A_s is the specific catalyst area available for surface reactions. The species molar flux J_k in the porous bed is evaluated using the Dusty-Gas Model (DGM) equation as

$$J_k = -\left[\sum_{l=1}^{K_g} D_{kl}^{DGM}\nabla[X_l] + \left(\sum_{l=1}^{K_g} \frac{D_{kl}^{DGM}[X_l]}{D_{l,Kn}^e}\right)\frac{B_g}{\mu}\nabla p\right] \qquad [22]$$

The DGM is written as an implicit relationship between the pressure gradient, concentration gradients, molar fluxes, binary diffusion coefficients and Knudsen diffusion coefficients. The first term on the right-hand side of Eq. [22] represents the diffusive flux and the second term represents the viscous flux. D_{kl}^{DGM} is defined as DGM diffusion coefficients. Further details about the solution procedure and model can be found in our previous publications (4, 6). In order to solve the second order boundary value problem, i.e., Eq. [20], boundary conditions are required at the electrode-channel and electrode-electrolyte interface. At the electrode–gas chamber interface the inlet mass fractions serve as the boundary condition, while at the electrode–electrolyte interface the species fluxes are zero. The electrochemical reaction source terms, for electrochemically active species, are calculated from the current density and are accounted for along with the chemical source terms. Thus, at the electrode–electrolyte interface, the molar fluxes of H_2, CO and O_2 can be given as

$$J_{H_2O} = -J_{H_2} = \frac{I_{H_2}}{2F}, J_{CO_2} = -J_{co} = \frac{I_{CO}}{2F}, J_{O2} = -\frac{\left(I_{H_2} + I_{CO}\right)}{4F} \qquad [23]$$

The computational procedure of the button cell model is well elucidated in (7). The entire code is written in FORTRAN and is a part of the detailed chemistry software package DETCHEM^{TM} (8). The equation system is solved using the differential algebraic equation (DAE) solver LIMEX (9).

Results and Discussion

The model is validated with experiments performed by Ebbesen et al. (10). The aim of their study was to investigate the reaction pathways involved during the co-electrolysis of H_2O and CO_2 as well as oxidation of H_2 and CO in different fuel mixtures. In the experiments, they demonstrated reduction of H_2O and CO_2 as well as oxidation of H_2 and CO. The thicknesses of the NiO/YSZ porous support layer, NiO/YSZ hydrogen electrode, YSZ electrolyte and LSM/YSZ oxygen electrode were 300 μm, 10-15 μm, 10-15 μm and 15-20 μm respectively. The inlet flow rate of pure oxygen to the LSM/YSZ electrode was 20 l/h for all experiments. Leakage overpotentials could be considered in the potential balance equation if the difference between cell voltages, throughout experiment and simulation, at open-circuit is evident. The electrochemical model input parameters used for reproducing the experimental data are listed in Table I . The values of thicknesses of the electrodes, electrolyte, and cell properties used in the model validation are also listed in Table II . It is important to note that micro-structural properties are assumed due to its unavailability in the aforementioned literature.

TABLE I. Electrochemical Model/Input Parameters

Property	H$_2$ electrode	CO$_2$ electrode
Anode asymmetry factor (β_a)	0.7	0.5
Cathode asymmetry factor (β_c)	0.1	0.1
Exchange current density parameters		
Pre-exponential factor (k_i) (A/cm^2)	594113.8731	16129714.99
Activation energy (E_i) (J/mol)	108.4×10^3	131.38×10^3
Pre-exponential for O$_2$ production (k_{O2}) (A/cm^2)	41783.22453	
Activation energy for O$_2$ production (E_{O2}) (J/mol)	88.75×10^3	

TABLE II. SOFC Input Parameters and Material Properties

Parameter	Model validation
Anode	
Thickness (μm)	315
Porosity (%)	35
Tortuosity	5.0
Particle diameter (μm)	1.0
Pore diameter (μm)	0.22
Specific area (m^{-1})	1.025x10^5
Electrolyte	
Thickness (μm)	15
Cathode	
Thickness (μm)	20
Porosity (%)	35
Tortuosity	5.0
Particle diameter (μm)	1.0
Pore diameter (μm)	0.22
Specific area (m^{-1})	1.025x10^5
Operating conditions	
Pressure (bar)	1.0
Temperature (°C)	750 °C, 850 °C

Figure 2 shows good agreement between numerical simulation results and experimental data, measured at 750°C and 850°C with inlet gas compositions of 50% H$_2$O: 25% H$_2$: 25% Ar and 25% H$_2$O: 25% H$_2$: 50% Ar to the Ni/YSZ electrode. The numerical model over-predicts the potential at open-circuit. Due to this facet, the model under-predicts current density at a specified voltage for the latter fuel composition. Nevertheless, the model is able to qualitatively reproduce experimental data. The V-I curves appeared to be more sensitive to $i^*_{H_2}$ in the electrolysis mode, while $i^*_{O_2}$ was more sensitive in the fuel cell mode. Any potential below E_{rev} results in a switch from the electrolysis mode to the fuel cell mode of operation. In order to understand the variation in ionic and electronic fluxes at the anode, cathode and electrolyte, one can always resort to the distributed charge transfer model which considers electrochemical reactions to occur throughout the thickness of the electrode. The model also tends to predict limiting current behavior well. For 25% H$_2$O: 25% H$_2$: 50% Ar, the calculated Area Specific Resistance (ASR) values at 1.1 V are 0.323 Ω.cm^2 at 850 °C and 0.558 Ω.cm^2 at 750 °C. The ASR is calculated in the electrolysis mode of operation. It is vital to note that the ASR values slightly differ based on the mode of operation, i.e, electrolysis or fuel cell mode (10).
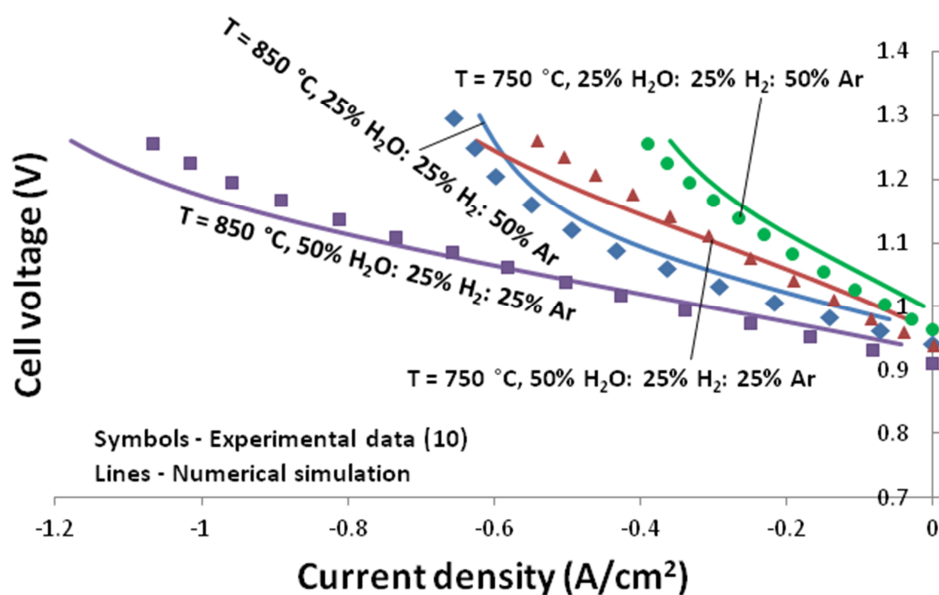
Figure 2. Comparison between numerical simulations and experimental data for H_2O-H_2-Ar mixtures.

Figure 3 shows excellent agreement between numerical simulation results and experimental data, measured at 750°C and 850°C with inlet gas compositions of 50% CO_2: 25% CO: 25% Ar and 25% CO_2: 25% CO: 50% Ar to the Ni/YSZ electrode. For 25% CO_2: 25% CO: 50% Ar, the calculated ASR values at 1.1 V are 0.397 $\Omega.cm^2$ at 850 °C and 0.725 $\Omega.cm^2$ at 750 °C. The ASR values for CO_2 electrolysis were higher than both steam electrolysis and co-electrolysis. This could be a consequence of simple diffusion rates of individual species. The model was more sensitive to exchange current density and charge transfer coefficients of the O_2 electrode as opposed to the CO_2 electrode.
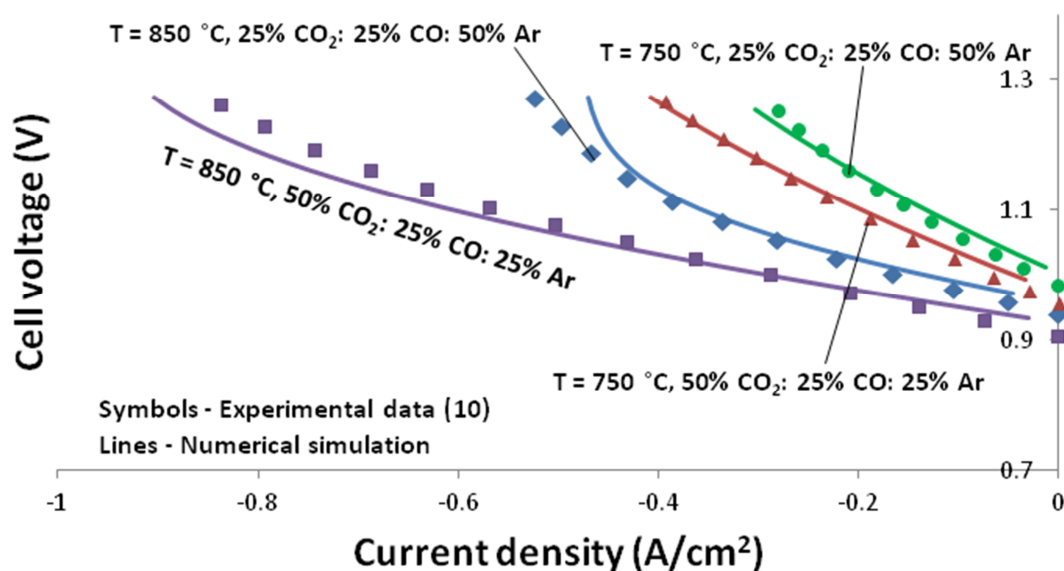

Figure 3. Comparison between numerical simulations and experimental data for CO_2-CO-Ar mixtures.

Figure 4 shows excellent agreement between numerical simulation results and experimental data, measured at 750°C and 850°C with an inlet gas composition of 25% H_2O: 25% CO_2: 25% CO: 25% Ar to the Ni/YSZ electrode. Initially, fits were made for H_2O and CO_2 based inlet gas compositions, individually, in order to determine electrochemical model input parameters. Then, simulations are carried for H_2O – CO_2 – H_2 – CO mixtures, after calibration. In order to account for differences in voltage at open-circuit, leakage overpotential is considered. This is given by

$$\eta_{leak} = \eta_{leak,max} \left(1 - \frac{i}{i_{max}}\right) \qquad [24]$$

where i_{max} is the maximum current. In this case, we use $\eta_{leak,max} = 0.03$ V and $i_{max} = 1.0$ A/cm^2. The calculated ASR values at 1.1 V are 0.275 Ω.cm^2 at 850 °C and 0.592 Ω.cm^2 at 750 °C. The ASR values correspond to the case where leakage losses are not considered. An addition of H_2O reduces the ASR, implying the participation of both H_2O and CO_2 during electrolysis at the TPB. This is because the ASR for H_2O electrolysis is lower than that of the ASR for CO_2 electrolysis. For further understanding, interested readers are directed to an exceptional article - (10). For model validation, i_i^* and β are adjusted to reproduce experimental data. However, it is important to bear in mind that these parameters are not unique. The two parallel electro-chemical reactions normalize to a single value of current density (also at open-circuit) via charge and mass conservation equations. The model is coupled with micro-kinetics, i.e., a 42-step elementary heterogeneous reaction mechanism is used at the cathode. The mechanism, along with the applied mean-field approach can be found in (7).
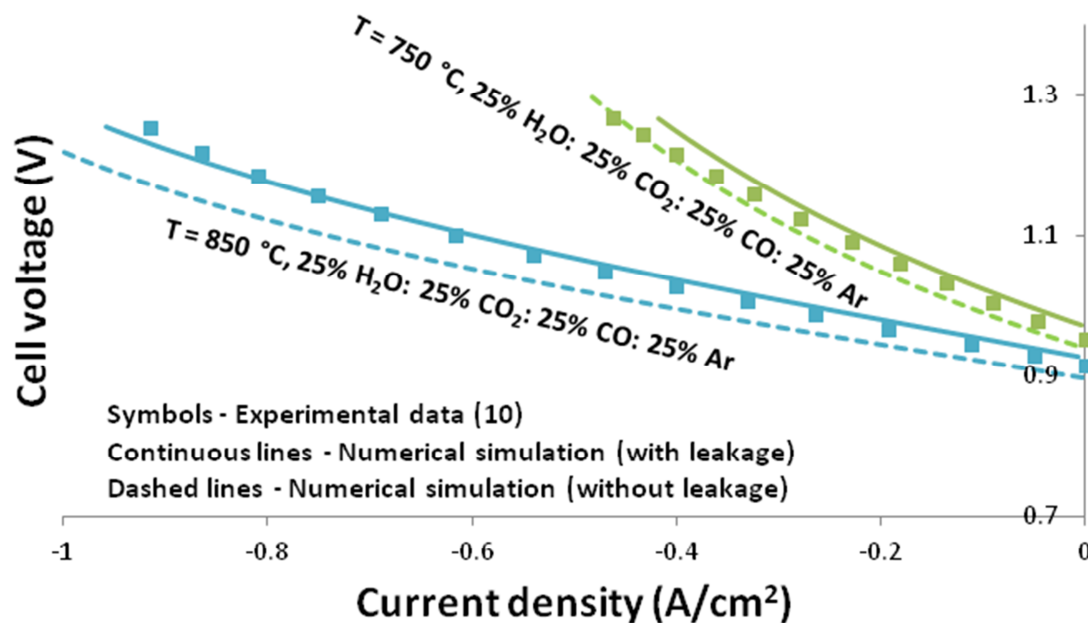

Figure 4. Comparison between numerical simulations and experimental data for H_2O-CO_2-H_2-CO-Ar mixtures.

In Figure 5, one can observe the variation in activation and ohmic overpotentials, during co-electrolysis, with current density. The overpotentials are simulated for the case where leakage overpotentials are not considered. The overpotentials decrease with an increase in temperature. It is important to remember that the current densities are actually

negative and only the magnitudes are considered for parametric analysis. An increase in temperature drastically improves the electrochemical performance of the cell. But, high temperature operation has two main disadvantages – (i) Cell degradation, and (ii) Cost of suitable materials. Thus, better thermal management techniques and/or materials that can operate at intermediate to high temperatures are required. The ohmic overpotentials decrease with increase in temperature as a result of Eqs. [10] and [11]. It is interesting to note that the activation overpotentials are greater at the cathode side as compared to the anode side. It is also known that the electrode performance is better when the cell is operating in co-electrolysis mode as compared to CO_2 electrolysis mode.
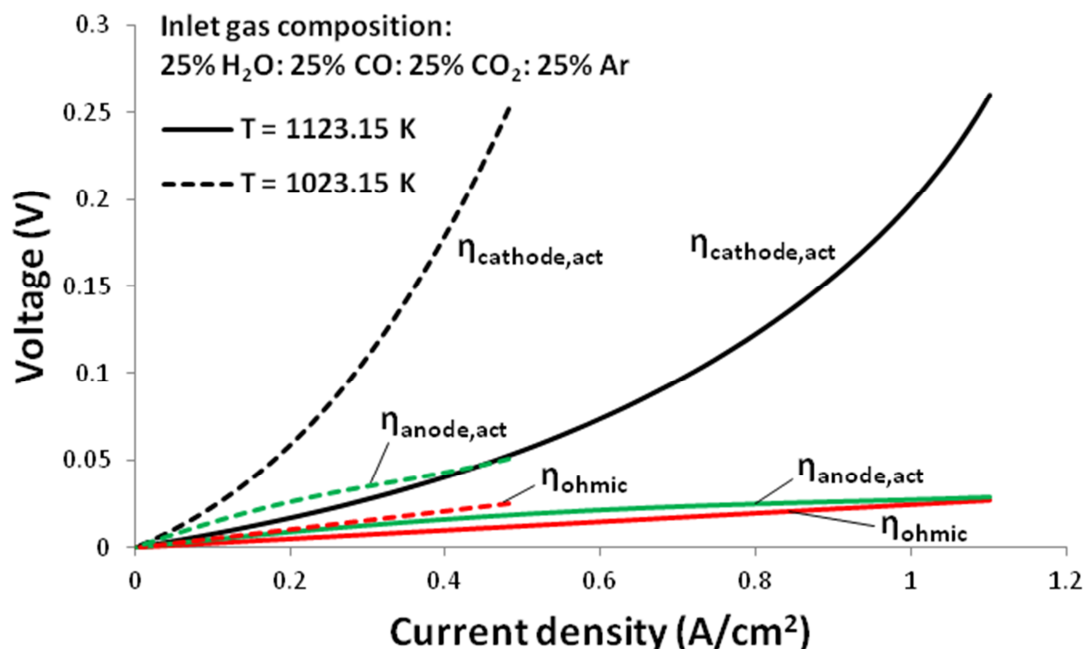

Figure 5. Evolution of irreversible losses, during co-electrolysis, with current density.

Conclusions

A detailed electrochemical model for H_2O and CO_2 co-electrolysis has been developed. The model uses Butler-Volmer equations for both H_2O and CO_2 electrolysis. It has the possibility for incorporation into other macro-scale models for further study of internal multi-physics phenomena. It also has been validated with experimental data available in literature. The electrochemical performance of the cathode proved to be better for co-electrolysis as compared to CO_2 electrolysis, based on ASR values. Further work would involve investigation into the possibility of the methanation reaction to take place under certain operating conditions, and to better understand the underlying charge transfer mechanisms of SOEC during co-electrolysis.

Acknowledgments

References

1. M. Ni, *J. Power Sources*, **202**, 209 (2012).
2. Y. Xie and X. Xue, *Solid State Ionics*, **224**, 64 (2012).
3. J. E. O'Brien, M. G. McKellar, C. M. Stoots, J. S. Herring, and G. L. Hawkes, *Int. J. Hydrogen Energy*, **34**, 4216 (2009).
4. H. Zhu, R. J. Kee, V. M. Janardhanan, O. Deutschmann, and D. G. Goodwin, *J. Electrochem. Soc.*, **152**, A2427 (2005).
5. G. Narasimhaiah and V. M. Janardhanan, *J. Solid State Electrochem.*, **17**, 2361 (2013).
6. V. Menon, V. M. Janardhanan, S. Tischer, and O. Deutschmann, *J. Power Sources*, **214**, 227 (2012).
7. V. M. Janardhanan and O. Deutschmann, *J. Power Sources*, **162**, 1192 (2006).
8. O. Deutschmann, S. Tischer, S. Kleditzsch, V. M. Janardhanan, C. Correa, D. Chatterjee, N. Mladenov, H. D. Mihn, and V. Menon, *DETCHEM^{TM} Software package -2.4 ed.*, http://www.detchem.com/, Karlsruhe 2012.
9. P. Deuflhardt and E. Hairer, *J. Zugk, Numer. Math.*, **51**, 501 (1987).
10. S. D. Ebbesen, R. Knibbe, and M. Mogensen, *J. Electrochem. Soc.*, **159**, F482 (2012).